ON THE SIGNAL-TO-NOISE RATIO IN IUE HIGH DISPERSION SPECTRA

DAVID S. LECKRONE[1]

Laboratory for Astronomy and Solar Physics
NASA, Goddard Space Flight Center

AND

SAUL J. ADELMAN[1]
Department of Physics
The Citadel

Received 1988 July _____

[1] Guest Investigator with the International Ultraviolet Explorer Satellite which is sponsored and operated by the National Aeronautics and Space Administration, by the Space Research Council of the United Kingdom, and by the European Space Agency; Guest Investigator at the Regional Data Analysis Facility of NASA Goddard Space Flight Center.

ABSTRACT

We describe an observational and data reduction technique which reduces both fixed pattern and random noise in fully extracted IUE high dispersion spectra. This involves the co-addition of a matrix of images taken at three offset positions in the large aperture and at various exposure levels in both the SWP and LWR cameras. A procedure is formulated which utilizes these observations to disentangle fixed pattern from random noise, allowing the average amplitude of each, within a given wavelength interval, to be estimated as a function of average flux number. We find that fixed pattern noise can be characterized by two components, an "additive" background, which dominates at low flux numbers, and a "multiplicative" component, which varies with flux number as a power law at medium and high signal levels. The derived random noise also exhibits a background component, which combines in quadrature with a term varying as the square root of the signal. The combined total noise, in absolute flux number units, increases linearly with increasing signal. The steepness of this variation increases toward shorter wavelengths in both cameras.

We provide curves which allow one to estimate the signal-to-noise ratio in individual spectra at the wavelengths investigated. The S/N in the continuum of well exposed stellar spectra varies from 10 to 20, depending on position in the spectral format. The co-addition procedure yields an improvement in S/N by factors ranging from 2.3 to 2.9. It is

becoming clear that fixed pattern noise is at least partly an artifact of geometric misregistration in the processing of IUE images. Its complete removal by improved data reduction methods would improve the S/N of individual images by factors between 1.5 and 3.0, and co-addition to diminish random noise would yield even greater gains in the quality of IUE data.

I. INTRODUCTION

Over the past several years we have undertaken a comprehensive program of elemental abundance analyses of sharp-lined early-type stars, combining high quality ground-based optical spectra with high dispersion ultraviolet spectra obtained with the IUE. Such spectroscopy, encompassing the wavelength range from about 1250 A to about 8000 A, provides access to a larger range of excitation and ionization states and gives more thorough coverage of the periodic table than is possible with ground-based spectra alone. To assure uniformity of the abundance results obtained over this wide wavelength range, the quality of the ultraviolet spectra should be as good as that of the optical spectra. As the ultraviolet spectra are substantially more complex than their optical counterparts, if possible one would want a superior signal-to-noise ratio (S/N) and superior resolution in the ultraviolet.

Virtually every spectral feature seen in IUE spectra of sharp-lined B and A stars is a blend. In principle the shape and structure of a feature can yield clues about the identity and strengths of the contributors to the blend, if the S/N is sufficiently large. Alternatively, if one has reasonably accurate knowledge of the S/N of the data, one can at least distinguish between fluctuations in a line profile due to noise and those due to blending contamination.

Continuum placement is also sensitive to S/N. Rarely does one observe the line-free ultraviolet continuum in these stars. The "high points" in

the spectrum, corresponding to minima in the spectral line density, generally approach to within 5-10% of the line-free continuum at IUE resolution in stars with v sin i < 25 km s^{-1}. From spectrum synthesis of intervals around "high points", we can estimate the position of the line-free continuum, if the S/N is sufficiently high, and if we can make a reasonable prediction of the local S/N value. We then statistically evaluate the most probable maximum upward fluctuation of noise superimposed on a synthetic spectrum and use this to place the continuum with respect to the observed "high points".

Our original approach to maximizing the S/N of high dispersion IUE spectra, while trying to preserve the full spectral resolution of the instrument, was simply to average together large numbers of images observed with the small aperture. This was done for the stars ν Cap (B9 V), 134 Tau (B9.5 V) and π Cet (B7 V). Such co-addition did not yield the full improvement in S/N we expected. We had re-discovered what had already been noted by West and Shuttleworth (1981) and by York and Jura (1982), that IUE extracted spectral fluxes are degraded by point-to-point variations that are spatially fixed within the image format and which, therefore, cannot be reduced by the simple averaging of spectra taken at a given location within the format. This phenomenon is commonly called "fixed pattern noise" (FPN). Subsequently, we developed a simple observational and data reduction technique to partially "randomize" the FPN so that its amplitude would be reduced by averaging spectra together. The technique involves observing the target star at several different locations in the large aperture. This displaces the pattern of

FPN with respect to the stellar line spectrum, so that subsequent registration and averaging of the observed spectra reduces the amplitude of FPN roughly by the square root of the number of different offset positions employed. We have used this technique to produce high quality, co-added spectra for the chemically peculiar HgMn stars ι CrB and κ Cnc, for the field horizontal branch A star HD 109995, and for the normal stars θ Leo (A2 V), o Peg (A1 IV), 21 Aql (B7 IV), ξ Oct (B6 IV), ι Her (B3 IV), HR 1886 (B1 V) and HR 1887 (B0.5 V), the latter four in collaboration with Dr. G. J. Peters. In §II we describe the observational and data reduction techniques in more detail and present empirical values of S/N achieved.

Observing the same spectrum at different positions in the image format provides a basis both for disentangling FPN from random noise (RN) and for extracting statistical information about the magnitude of FPN and RN as a function of the flux level of the extracted spectrum. If we were setting out specifically to investigate the properties of FPN and RN in IUE spectra, we would not have selected sharp-lined, early type stars as the preferred targets. Rather, ideal targets would be stars with flat and smooth ultraviolet flux distributions. However, our principal objective is to derive elemental abundances in astrophysically interesting objects and we investigate the noise properties of the data only to lay the foundation for accurate spectrum synthesis. It is a serendipitous result of the observing technique that we are able to ascertain some gross properties of the noise in our data. In §III we provide a schematic description of the simple noise model employed. The

Appendix outlines the derivation of the numerical algorithms used to calculate the average amplitudes of RN and FPN in individual orders of individual spectra. The detailed analysis of our data, qualitative relationships, and numerical results are described in §IV. Section V provides a summary and comparison with the work of others. The present study supersedes an earlier effort by Adelman and Leckrone (1985), as it is based on a more rigorous formulation of the noise model.

II. OBSERVATIONS AND DATA REDUCTION

To obtain acceptable exposure densities over the entire wavelength range of the LWR and SWP cameras for the "cool" flux distributions of our late B and early A-type targets, it was necessary to obtain three exposures (of short, medium and long duration) of each star in each camera. To "randomize" the fixed pattern noise in the observed spectra, we obtained exposures at three positions in the 10 arcsec by 20 arcsec large aperture of each spectrograph. In fine error sensor coordinates these positions were (+5,-208), (-16,-208) and (-37,-208). Thus, a typical set of exposures for a given star consisted of a 3x3 matrix of images obtained in each camera.

The analyses in this paper are based primarily on the observations of θ Leo, o Peg, and 21 Aql listed in Table 1. Table 1 also gives the measured relative radial velocity shift for each observation, corresponding to the offset position in the large aperture plus the relative shift due to the spacecraft's velocity. These are measured relative to a single (-16,-208) image in each camera for each star, selected as a fiducial. The relative offsets of the spectra within each set span about 60 km s^{-1} on average, which corresponds to a spatial offset in the camera format of approximately 8 pixels, or about 11 sample points (since standard IUE data reduction uses an analyzing slit $\sqrt{2}/2$ pixels wide). Thus, the co-registration of spectra taken at these three nominal offset positions, by alignment of stellar lines, should

produce complete de-correlation of "fixed pattern" features which are narrower than about four pixels (six samples) and significant partial de-correlation of features up to, say, twice that width. Coincidentally, the earth's orbital velocity is about 30 km s^{-1}. Therefore, a similar degree of de-correlation of FPN will be seen in small aperture observations of a target within about ±25 degrees of the ecliptic, if it has been observed at well chosen times spread over half a year.

The variations in the velocity shifts at each nominal offset position in Table 1 are due primarily to differential spacecraft orbital velocities among the various observations. These range from a few tenths of a km s^{-1} up to nearly 10 km s^{-1}. These differential velocities produce small displacements in offset position from spectrum-to-spectrum, which serve to de-correlate high frequency fixed pattern noise among images taken near the same offset position. That is, at least partial de-correlation will occur along the exposure level dimension, as well as along the spatial offset dimension, of a 3x3 matrix of images. Nichols-Bohlin (1988) has shown that FPN is pronounced at the highest spatial frequencies in IUE images.

The data were reduced using the facilities of the IUE Regional Data Analysis Facility at the Goddard Space Flight Center. The matrix of extracted spectra obtained for an individual star in one camera was aligned, using a cross-correlation routine, and coincident sample points were obtained by interpolation. In averaging, each sample point was weighted by the exposure time of the image and by a factor that depends

on the value of the data quality flag, ϵ. Sample points affected by extrapolation of the upper end of the intensity transfer function (ITF) were weighted by 0.1; those affected by microphonic noise, bright spots or reseaus were weighted by 0.001; and those involving saturated pixels or excessive ITF extrapolation were rejected entirely. There are several advantages to this procedure. Even overexposed orders, such as those at long wavelengths in medium and long integrations, often contain many well-exposed pixels within the cores of spectral lines, which can greatly enhance the overall S/N in the line cores of averaged spectra. In spectra that are obtained at different offset positions in the format, reseaus and bright pixels affect different wavelengths. The effect of reseaus and bright pixels in co-added data, therefore, is to reduce the S/N in short segments of the spectrum. Only rarely is it necessary to omit a sample point from an averaged spectrum because all of the individual spectra contributing to the average at that point were affected by a reseau or a bright pixel.

In Figure 1 we compare a segment of the spectrum of the B7 V star π Cet, near the Si II (UV2) lines $\lambda\lambda$ 1526, 1533, obtained from a single well-exposed small aperture image, SWP 16248, to an average of nine small aperture images of this star. Subjectively, there appears to be only a slight improvement in the "noisiness" of the spectrum in the average. In contrast Figure 2 illustrates for the B7 IV star 21 Aql a marked improvement in overall noise level achieved by averaging nine images obtained at three different offset positions in the large aperture, as previously described.

A more quantitative indication of the S/N achieved in our averaged, large aperture spectra is given by the data in Table 2. Two of our program stars, the metal-deficient field horizontal branch A star HD 109995 and the B7 IV star 21 Aql, are relatively weak-lined in the ultraviolet. In their spectra one occasionally encounters wavelength intervals, ranging from about half an Angstrom to about two Angstroms in width, in which the stellar flux distributions remain high, flat and more or less unstructured. We believe these are line-free windows in which the flux reaches the true continuum. The point-to-point fluctuations in the signal in these intervals gives a direct measure of its standard deviation (σ) and thus of the S/N. The measured values of σ at various wavelengths are listed in Table 2, together with the number of spectra averaged in each case. Note that in two long-wavelength SWP orders for 21 Aql the data become remarkably smooth (S/N $\simeq$ 125!). This may result from a slight defocusing of the SWP camera at an edge of its format in which a portion of several long wavelength orders falls. The data in Table 2 will be used as benchmarks to evaluate the noise estimates derived in the sections that follow.

III. THE NOISE MODEL

Our observational technique for improving the S/N of high dispersion spectra involves the positional offset of each stellar spectrum relative to the fixed noise background. We use the data so obtained to disentangle random and fixed pattern noise and to derive rough, quantitative estimates of how the amplitude of each varies as a function of the average exposure level of an individual order. The following discussion gives a simple, conceptual framework for understanding the analysis. The algorithms derived on the basis of this model are summarised in the Appendix. Throughout this discussion we denote with $\underline{a}$ and $\underline{b}$, respectively, the standard deviations of fluctuations due to FPN and RN in a specified wavelength interval within a single order of a fully extracted spectrum. We assume both FPN and RN obey Gaussian statistics, so that the two can be combined in quadrature.

Consider the three spectra shown in Figure 3A. These correspond to three images of approximately the same exposure level, taken at three offset positions in the large aperture, denoted by C (center), L (left) and R (right). They represent a cut through our idealized 3x3 matrix of images along the offset-position dimension. The "X" in each spectrum is a fiducial which is fixed with reference to the stellar line spectrum (which is otherwise not illustrated, for simplicity). The arrows are fluctuations due to fixed-pattern noise. Their direction and size were chosen randomly. Random noise is not illustrated, again for simplicity.

Note that the pattern of arrow sizes and directions is spatially fixed relative to the camera format, and the stellar spectrum (the "X") is displaced in position with respect to the FPN pattern, from image to image. In sections B and C of Figure 3 we align the stellar line spectrum in the three images and average the three together. This decorrelates the FPN fluctuations and causes their standard deviation to be reduced (the fact that they are not reduced by exactly $\sqrt{3}$ is an artifact of the small size and differing end points of the three illustrative spectra). If we now subtract the average spectrum from each original spectrum, we obtain the "first difference spectra" shown in Figure 3D. The stellar line spectrum is no longer apparent in a first difference spectrum. Rather the point-to-point variations are due to some combination of RN and FPN. Random noise is greater than in the original spectra and, as illustrated in Figure 3D, FPN is reduced somewhat in amplitude relative to the original spectra. Stated another way, the standard deviation, σ_1, of a first difference spectrum contains a component, σ_{r1}, due to RN and a component, σ_{f1}, due to FPN, so that

$$\sigma_1 = \sqrt{(\sigma_{r1}^2 + \sigma_{f1}^2)}. \qquad (1)$$

The random errors combine so that

$$\sigma_{r1} = \sqrt{(b^2 + \langle b \rangle^2)} > b, \qquad (2)$$

where $\langle b \rangle$ is the standard deviation due to RN in the average spectrum. An expression for σ_{f1} in terms of $\underline{a}$ and $\langle a \rangle$, the standard deviation due to FPN in the average spectrum, is given in equation A14. A typical first difference spectrum is illustrated in Figure 4. The quantity σ_1 is measured as the standard deviation of fluctuations about a linear least-squares fit through the observed first difference spectrum.

The next step in our procedure is illustrated in Figures 3E, F, and G. In Figure 3E each of the three first difference spectra have been displaced back to the original positions of Figure 3A. The remnants of the pattern of FPN should now be re-aligned. There should be a strong correlation from image-to-image between FPN fluctuations at a given sample point, as is evident by inspection of Figure 3E. When we average the first difference spectra (Figure 3F), this pattern of correlated points is emphasized. Subtracting the average from each individual first difference spectrum results in the "second difference spectra" of Figure 3G, in which the amplitude of FPN has been greatly reduced. Thus, the measured standard deviation, σ_2, of a second difference spectrum is strongly dominated by RN and contains only a small contribution due to FPN. Specifically,

$$\sigma_2 = \sqrt{(\sigma_{r2}^2 + \sigma_{f2}^2)}, \tag{3}$$

where

$$\sigma_{r2} = \sqrt{(b^2 + \langle b \rangle^2 + \langle \sigma_{r1} \rangle^2)}, \tag{4}$$

and $\langle \sigma_{r1} \rangle$ is the standard deviation due to RN in the average first difference spectrum. An expression for σ_{f2} in terms of $\underline{a}$ and $\langle a \rangle$ is given in equation A30. The quantity σ_{f2} is measured as the standard deviation about a linear fit through the observed second difference spectrum.

The data analysis procedure illustrated in Figure 3 produces two measured quantities, σ_1 and σ_2, which can be expressed as relatively simple functions of $\underline{a}$ and $\underline{b}$. Thus, one can solve simultaneously for $\underline{a}$ and $\underline{b}$ in each observation to obtain an estimate of the amplitudes of FPN

and RN, averaged over the specified wavelength interval and over the range of fluxes spanned by the stellar spectrum in this interval. The values of σ_1 and σ_2 actually measured at various average exposure levels for two SWP and two LWR orders in our three program stars are plotted in Figures 5 and 6.

The algorithm needed to derive a and b from σ_1 and σ_2 evolved from the simple to the complex. Algorithm I algebraically represented the various steps illustrated in Figure 3. However, it ignored any variations of a as a function of exposure level. It did not realistically calculate averages and difference spectra amplitudes for a full 3x3 matrix of spectra taken at different exposure levels. But it converged rapidly to a unique set of values for a and b. Algorithm II took full account of the two-dimensional nature of the problem. Initially, it did not converge well and it was modified to use preliminary values of a calculated from Algorithm I to set approximate values for ratios of a among weak, medium and strong exposures. Both algorithms assumed that spectra taken at the same nominal offset position (i.e. images at different exposure levels) were identically aligned on the camera format, so that cross-correlating and averaging such images produced no reduction in FPN. Both yielded predicted noise levels in averaged spectra which were considerably higher than we actually observed in the co-added data (Table 2). We attribute this to relative misalignments of order ±1 sample point in spectra taken at the same nominal spatial offset, due primarily to differences in spacecraft velocity. Nichols-Bohlin (1988) has shown that FPN appears to be a high frequency

phenomenon, so that averaging spectra over both the exposure-level dimension and the offset position dimension in our 3x3 matrix could statistically reduce the FPN amplitude by a factor approaching $1/\sqrt{9}$. Therefore, we developed Algorithm III which assumes full decorrelation of FPN in both dimensions when the nine stellar spectra are cross-correlated and averaged and when the first difference spectra are calculated (Figures 3B, C and D). Second difference spectra, however, are perfectly correlated, by definition, and are treated the same way in Algorithms II and III.

Algorithm III produces calculated values of $\sqrt{(a^2 + b^2)}$ for the co-added spectra which are reasonably consistent with the observations. We can see why by careful inspection of the specific relative offset numbers for any star/camera combination in Table 1. Typically, out of nine pairs of images which could be correlated along the exposure-level dimension (three pairs at each offset position), at least six pairs tend to be separated in velocity by 0.5 to 1.0 sample intervals or more. Thus, we are closer to the condition of complete de-correlation than to that of complete correlation in the observations and Algorithm III is a better approximation to reality than Algorithm II. (In future observing programs we would recommend adopting nine different offset positions, separated by at least one sample interval, ~ 5 km s^{-1}, to guarantee full de-correlation.) All three algorithms yielded qualitatively similar results for the distributions of $\underline{a}$ and $\underline{b}$ as a function of average exposure level. Average noise levels calculated with Algorithm II and Algorithm III are compared in §IV.

IV. ANALYSIS

A complete noise analysis was carried out for two SWP orders, 83 and 93, and for two LWR orders, 96 and 102. Within each order only the central wavelength interval of maximum exposure density was measured. These particular orders were selected because their exposure density fell within a useable range for all nine images in the 3x3 matrix for all three program stars, 21 Aql, θ Leo and o Peg. At longer wavelengths some images were too heavily exposed, at shorter wavelengths some were too lightly exposed. Partially complete sets of data were analysed for a few additional orders - for example, a complete 3x3 matrix in SWP 88 (1555 -1575 A) for o Peg and incomplete matrices for all three stars in SWP 80 (1716 - 1735 A). These are not illustrated in the following discussion for brevity, but they produced results very similar to those obtained from the four primary orders under consideration. Clearly our detailed quantitative results apply only to a limited portion of the image format of each camera, but the qualitative conclusions drawn are in all liklihood generally valid, considering our good agreement with the work of others described in §V. An observing program specifically intended to collect complete sets of useable images at the wavelengths of greatest and least sensitivity in each camera would be required to verify this with certainty. We also caution that our results pertain to relatively short exposure times on bright stars, which yield high signal levels against a minimal background. Moreover, quantitative noise values apply to data which have been smoothed over three sample points (approximately two pixels).

Figures 5 and 6 show the measured standard deviations, σ_1 and σ_2, of the first and second difference spectra, respectively, in the four orders as a function of measured average flux number, <FN>. These purely empirical plots reveal an important property of the noise in extracted spectra. As one approaches small flux numbers, the noise-to-signal ratio becomes quite large. This indicates the presence of a background noise component which becomes relatively more important as the net extracted flux approaches zero. The IUESIPS data processing system (Turnrose and Thompson 1984) heavily smoothes the background before subtracting it from the gross flux. Therefore, pixel-to-pixel noise fluctuations in the background are not removed and will be evident in the net extracted spectra. For example in the core of a fully saturated absorption line one expects noise fluctuations below and above the zero net flux level, yielding an infinite effective noise-to-signal ratio. However, particularly in the LWR spectra, the noise-to-signal ratio rises asymptotically toward infinity not at <FN>=0, but at <FN>≈7000 for order 96 and <FN>≈3500 for order 102. This becomes especially evident in the discussion of the derived random noise values that follows. It suggests the possibility of a zero-point flux-scale error somewhere in the standard data processing chain. We cannot preclude the possiblity of smaller errors of this kind in the SWP data as well.

The values of σ_1 and σ_2 shown in Figures 5 and 6 were inserted in Equations A45 and A46, which were then solved iteratively to derive the corresponding values of $\underline{a}$ and $\underline{b}$. These are plotted as a function of <FN>

in Figures 7 and 9. The quantities a and b are unitless, fractional noise-to-signal ratios. In the discussion of the properties of FPN and RN that follows we also present results as noise amplitudes in absolute FN units. That is

$$\langle FPN \rangle = a \cdot \langle FN \rangle, \quad \langle RN \rangle = b \cdot \langle FN \rangle, \tag{5}$$

where the averages are taken over designated wavelength intervals within specific orders.

From Figure 7 we see that a decreases monotonically with <FN>, although there is considerable scatter in the plots. The data for SWP 93 (and for o Peg, SWP 88, not illustrated here) extend to sufficiently low <FN> that we clearly see the presence of a background component of FPN which dominates in weak exposures. As exposure density increases, the functional relation of a versus <FN> tends to level out, that is a varies weakly with <FN> and, roughly, <FPN> ~ <FN>. The behavior of fixed pattern noise as a function of flux number is more clearly illustrated in log-log plots of <FPN> versus <FN>. Such plots for our four primary orders are illustrated in Figure 8. In the SWP 93 plot in Figure 8 a bifurcation is evident near <FN> = 8000. At smaller <FN> values the background noise dominates. At larger <FN>, log <FPN> varies linearly with log <FN>; that is FPN is a signal-dependent, power law function. We assume these two noise components combine in quadrature, so that

$$\langle FPN \rangle = \sqrt{(P^2 + Q^2 \langle FN \rangle^{2R})}. \tag{6}$$

The corresponding relation for a is obtained by dividing Equation 6 by <FN>. In the three other orders the data do not extend to sufficiently small <FN> to allow the bifurcation to be seen and only the power-law component is evident in Figure 8. Least squares fits to the log <FPN> versus log <FN> data yield the linear fits illustrated in Figure 8 and the fitting parameters in Table 3. The corresponding best-fit relations of a versus <FN> are plotted as dashed curves in Figure 7. Note that the best fit (by eye) for SWP 93 in Figure 7 explicitly includes the contribution of the residual background, while for the other orders, in which the background is not directly observed, its contribution is subsumed in the parameters derived from the least-squares fit to the power-law component. One can get an idea of the differences between these two cases from the entries for SWP 93 in Table 3.

For random noise one would expect a priori that two components should contribute in quadrature, the residual background and a component that varies as the square root of the signal (photon noise). That is

$$\langle RN \rangle = \sqrt{(B^2 + A^2 \langle FN \rangle)}. \qquad (7)$$

The corresponding relation for the fractional random noise, b, is obtained by dividing equation 7 by <FN>. The dashed curves in Figure 9 are reasonable compromise fits to the observed b versus <FN> data. The data for both SWP 93 and SWP 83 are fit with B = 700 and A = 5, suggesting that the residual RN background is roughly the same at these

two positions in the image format. Orders LWR 102 and LWR 96 are also well fit with this same function and the same values of B and A, but only if the <FN> zero-point is shifted by 3500 and 7000 FN units, respectively. That is, in b = <RN>/<FN> one must substitute <FN> ≃ 3500 for LWR 102 and <FN> ≃ 7000 for LWR 96 in place of <FN> in both the numerator and the denominator in order to achieve the fits shown in Figure 9. Otherwise it was not possible to fit the two LWR RN relationships with any function of the form of Equation 7, for example by varying the background term dramatically. As discussed previously, this suggests a zero point shift in the FN scale of the LWR data somewhere in the data processing chain. It is gratifying, however, that the values of b derived with our algorithm behave as random noise should, as illustrated by the rather good fits achieved in Figure 9.

Combining <FPN> and <RN> in quadrature, we obtain the total noise in FN units, which is plotted versus <FN> in Figure 10. To within the scatter in the data the total noise increases linearly with flux number for all four orders investigated. That is,

$$\sqrt{(\langle FPN\rangle^2 + \langle RN\rangle^2)} = D + E\langle FN\rangle. \qquad (8)$$

Linear least squares fits to the data are shown in Figure 10, and the corresponding fitting parameters are given in Table 4. The dashed curves in Figure 10 (to which the right hand vertical scale applies) give the total fractional noise-to-signal ratio obtained by dividing Equation 8 by <FN>. Since the relation between average total noise and average flux

number is linear (where averages are taken over a wide range of fluxes within the stellar spectrum), it is simple to show that the relationship between total noise and flux number for individual sample points (at discrete flux levels) must be approximately the same linear function. That is, by analogy to Equation 8,

$$\sqrt{(FPN^2 + RN^2)} = D + E \cdot FN, \qquad (9)$$

provided the sample points in the spectra used to derive Equation 8 are roughly uniformly distributed between the maximum and minimum flux numbers within those spectra (as we have assumed). Thus, Figure 10 can be used to evaluate the total noise-to-signal ratio at a particular flux level within an individual spectrum. The vertical arrows in Figure 10 denote our best estimates of the approximate <FN> values corresponding to optimally exposed spectra (whose brightest pixels are at 205-210 DN) for our three program stars in these orders. At these <FN> values the total signal-to-noise ratios range from about 17 in SWP 83 to about 9 in SWP 93. At these wavelengths the ratio of the mean flux to the maximum flux (i.e. to the continuum flux) is measured to be about 0.8 for 21 Aql and in the range 0.6-0.7 for o Peg and θ Leo. If we adopt 0.7 as a characteristic ratio, then the signal-to-noise ratio in the continuum is about 10 in SWP 93, 11 in LWR 102, 14 in LWR 96 and 20 in SWP 83, in a well exposed single image.

We now investigate what total noise levels are to be expected in a co-added 3x3 matrix of spectra. Table 5 lists values of <a> and <b>,

calculated with Algorithm II (complete correlation of the FPN pattern along the exposure level dimension) and with Algorithm III (complete decorrelation of FPN). As discussed in §III, our observations appear to be more closely represented by the assumptions of Algorithm III. Clearly Algorithm III yields substatially lower total noise than Algorithm II.

To compare the calculated noise to the empirically measured noise values of Table 2, we project the average calculated figures to the values they would have at the flux level of the continuum in Table 6. Column 4 in Table 6 lists the measured ratio of average flux to continuum flux in each wavelength interval. Dividing these ratios into the <FN> values in column 3 to obtain the approximate continuum FN values, we then use the noise-to-signal curves in Figure 10 to estimate the ratios of total noise in the continuum to total noise at the mean flux level, column 5 of Table 6. Multiplying the latter by the average total noise values in Table 5, results in the estimated noise in the continuum, columns 6 and 7 of Table 6. The noise levels calculated with Algorithm II are significantly higher than the observed values given in Table 2. For this reason, as well as for others discussed previously, we shall rely on the calculations of Algorithm III.

Comparing the total noise for 21 Aql and o Peg in the 1651 - 1670 A interval in Table 6 with the values directly observed for 21 Aql and HD109995 in the 1600 - 1700 A region (Table 2) we find good agreement. Similarly the derived noise for o Peg in the 1555 - 1575 A interval (Table 6) is consistent with the value observed near 1573 A in 21 Aql

(Table 2). The values derived for the 1474 - 1488 A region in all three program stars (Table 6) are somewhat larger than the values directly observed below 1500 A in 21 Aql (Table 2). The data of Table 2 were obtained from very narrow wavelength intervals and we have no way of assessing how accurately they represent the average noise over the much wider wavelength intervals covered by the observations used for Table 6. Unfortunately, the LWR data in Table 2 do not extend to sufficiently short wavelengths to allow a meaningful direct comparison with Table 6. It is fair to conclude from the derived noise values listed in Table 6, that signal-to-noise ratios ranging from about 22 to about 59 are achieved in these specific wavelength intervals in co-added spectra obtained using our techniques. The values listed in Table 2 suggest that we may be achieving somewhat better values than that in some places. This corresponds to an improvement in S/N by factors ranging from 2.3 to 2.9, compared to well exposed individual spectra.

V. SUMMARY AND DISCUSSION

In this paper we have described an observational and data reduction technique which reduces both fixed pattern and random noise in fully extracted IUE high dispersion spectra, yielding an improvement in signal-to-noise ratio by factors ranging from 2.3 to 2.9 for the specific cases considered. This technique also provides a means to disentangle fixed pattern from random noise, so that the average amplitudes of each, within a given wavelength interval, can be estimated as a function of average flux number. Thus, we are able to assess the qualitative behavior of the two noise sources, and of the total noise, as well as make quantitative estimates of their magnitudes.

Fixed pattern noise appears to have two components: an "additive" background, which is a remnant of the subtraction of heavily smoothed interorder noise; and a "multiplicative" component, which varies as flux number to some power of order 0.7-1.0. At low FN the additive background dominates; at higher FN the fixed pattern noise amplitude varies linearly in a log<FPN> versus log<FN> plot. Linde and Dravins (1988) demonstrated that FPN can be substantially reduced by improving the geometric registration between IUE spectral images and the flat-field images used to derive pixel-by-pixel intensity transfer functions. That is, FPN can be regarded as error produced by systematically applying incorrect ITF's to each pixel. If so, then the "multiplicative" nature

incorrect ITF, which is erroneously applied, diverge, producing larger errors the higher the level of exposure. Alternatively, the source of FPN may reside partly within the instrument itself. In this case the elucidation of its character by the present study should provide clues about its origin.

The estimated random noise derived from our data appears to behave as one would expect. A remnant point-to-point random background fluctuation, left over from the background subtraction process, combines in quadrature with a component that varies as the square root of the signal. In our measurements of the standard deviations of first and second difference spectra, and particularly in our analysis of RN, we find evidence that a zero-point error in the assigned flux numbers has been introduced somewhere in the data processing chain, most obviously in the data for the LWR camera.

Combining our estimates of fixed pattern and random noise amplitudes, we find that total noise (in flux number units) increases linearly with increasing flux number. This makes it simple to convert the relationship between <FPN> and <FN> to a relationship between FPN and FN - they are approximately the same linear function. On the basis of two SWP and two LWR orders, the slope of this function appears to increase with decreasing wavelength in both cameras. Kinney, Bohlin, and Neill (1988) have directly measured the variance in flux number as a function of average flux number within 26x26 pixel or 13x26 pixel patches distributed around numerous low dispersion spectra obtained with the

SWP, LWR and LWP cameras. They also find linear relations between total noise and flux number. Their measured slopes also decrease with increasing wavelength in SWP and in LWP. However, they do not find such a variation in slope in LWR, a minor contradiction which may reflect the fact that we are measuring different segments of the camera format. Quantitatively, our measured slopes (E in Table 4) are in rough agreement with those of Kinney, et al., and our background terms (D in Table 4) are also reasonably consistent when one takes into account that the measurements refer to different sample dimensions (individual pixels in their data, slit dimensions approximately 6 by $\sqrt{2}/2$ pixels in ours), and that our measurements are averaged over three sample widths. One would expect the background noise to be larger in our high dispersion spectra because of interorder scattered light in the echelle format and that seems to be the case (by a factor $\simeq 2$). In any event our two very different observational and data reduction techniques yield gratifyingly similar results for the behavior of total noise as a function of FN.

Our results (Figure 10) and those of Kinney, et al., demonstrate that as exposure levels become small, the total noise-to-signal ratio in IUE spectra rapidly rises to levels which are probably unacceptable for most interpretative purposes, because of the residual background component. Thus, one should be wary in attempting to extract information from weakly exposed images.

The signal-to-noise ratio achieved in the continuum of a single, well-exposed IUE stellar spectrum varies with position in the spectral

format. For the specific wavelength regions addressed in this study, regions of intermediate sensitivity, we find S/N ≃ 10-20. If FPN could be removed from such individual images by means of improvements in data processing (for example, by a more accurate geometrical registration), the residual random noise in the continuum would be about 0.034 or S/N ≃ 29, based on Figure 9. Such an improvement in signal-to-noise ratio by a factor of about 1.5 to 3.0, with even larger improvements realized in those cases where multiple images can be co-added to reduce random noise, would greatly enhance the scientific value of IUE data.

ACKNOWLEDGEMENTS

We thank the IUE and Goddard RDAF staffs, in particular Mrs. Rosalie Ewald and Mr. Keith Feggans, for their assistance in this investigation and Drs. Joy Nichols-Bohlin and Cathy Imhoff for useful discussions. The cross-correlation routine used was originally written by Dr. Sidney Parsons and the co-addition routine by Dr. F. H. Schiffer, III.

APPENDIX

THE NOISE ALGORITHM

A. Random Noise

Equations 2 and 4 in Section III express the random noise component of the first and second difference spectra, respectively, in terms of b, <b> and $<\sigma_{rl}>$. Here the weighted average random noise amplitude in a co-added spectrum is

$$<b> = \frac{\sqrt{\sum C^2 <FN>^2 b^2}}{\sum C <FN>}, \tag{A1}$$

where the sums are over all spectra in the 3 x 3 matrix. The quantity <FN> is the average flux number in each spectrum and C is an empirically derived weight which depends on the quality of each spectrum, viz,

$$C = \frac{N(\epsilon=100) + 0.1N(\epsilon = 200) + 0.001N(200<\epsilon<900)}{N}, \tag{A2}$$

where the N-values are the number of sample points in the spectrum with the given quality flag ϵ-values and N is the total number of sample points in the spectrum. The random noise in the average of all nine first difference spectra is

$$<\sigma_{rl}> = 1/9 \sqrt{\sum(b^2 + <b>^2)}. \tag{A3}$$

B. Fixed Pattern Noise, First Difference Spectrum

The contribution of FPN to the noise of a first difference spectrum made up of N sample points is

$$\sigma_{fl} = \sqrt{\left[\sum_{i=1}^{N} (a_i - \langle a_i \rangle)^2/(N-1)\right]}. \qquad (A4)$$

Here, subscript $\underline{i}$ refers to sample points located with reference to the stellar spectrum (with reference to the fiducial $\underline{x}$ in Figure 3), independent of where in the camera format the spectrum was observed. The quantity a_i is the FPN fluctuation at sample point $\underline{i}$ in a single spectrum and $\langle a_i \rangle$ is the weighted average of FPN fluctuations at this sample point in the average spectrum (Figure 3C). Since the standard deviation due to FPN in a single spectrum, $\underline{a}$, is by definition

$$a = \sqrt{\left[\sum_{i=1}^{N} a_i^2/(N-1)\right]}, \qquad (A5)$$

and the FPN standard deviation in an average (co-added) spectrum is defined to be

$$\langle a \rangle = \sqrt{\left[\sum_{i=1}^{N} \langle a_i \rangle^2/(N-1)\right]}, \qquad (A6)$$

we can re-write Equation A4 as

$$\sigma_{fl}^2 = a^2 + \langle a \rangle^2 - 2\left[\sum_{i=1}^{N} a_i \langle a_i \rangle/(N-1)\right]. \qquad (A7)$$

The evaluation of the sum in Equation A7 depends upon one's assumption about whether or not different stellar spectra (at different exposure levels) taken at the same nominal offset point are identically aligned with respect to the background of FPN (so that their FPN fluctuations are perfectly correlated). As discussed in § III, the observational

evidence suggests they are largely misaligned (with decorrelated FPN fluctuations) on the scale of $\pm$ 1 sample point. We have developed a formalism for each case. We first describe the case of perfect correlation, then its simplification to the case of complete de-correlation. Note that this distinction between the two cases affects only the derivation of σ_{fl}. Second difference spectra are by definition perfectly aligned with respect to the FPN background.

For clarity, we use subscripts w, m and s to denote weak, medium and strong exposures; we use subscripts l, c and r to denote exposures spatially offset to left, center and right positions in the large aperture; and W, M and S denote the <u>average</u> weights (average of C<FN>) for weak, medium and strong exposures, respectively. For an idealized 3 x 3 matrix of images

$$\begin{aligned} \langle a_i \rangle = \frac{1}{3} \,(&Wa_{ilw} + Wa_{icw} + Wa_{irw} \\ &+ Ma_{ilm} + Ma_{icm} + Ma_{irm} \\ &+ Sa_{ils} + Sa_{ics} + Sa_{irs})/(W+M+S). \end{aligned} \tag{A8}$$

The expression $\sum a_i \langle a_i \rangle$ then contains nine terms, each a sum over N sample points, six of which should $\simeq 0$. Consider, for example, a "weak" exposure taken in the "left" position:

$$\begin{aligned} 2\left[\sum_{i=1}^{N} a_{ilw} \langle a_i \rangle/(N-1)\right] = \frac{2}{3}\Bigg[&W \sum_{i=1}^{N} a_{ilw}^2/(N-1) + M \sum_{i=1}^{N} a_{ilw} a_{ilm}/(N-1) \\ &+ S \sum_{i=1}^{N} a_{ilw} a_{ils}/(N-1)\Bigg]/(W+M+S). \end{aligned} \tag{A9}$$

Every other term in $\sum a_{ilw} \langle a_i \rangle$ involves factors which are totally uncorrelated. There is an equal chance that their product will be positive or negative, and statisically their sum over a large number of sample points will vanish.

Evaluation of Equation A9 becomes tractable only if we can assume that on average

$$a_{ilm}/a_{ilw} \simeq a_m/a_w \equiv f, \tag{A10}$$

where a_m and a_w are defined by Equation A5 for a medium exposure and a weak exposure, respectively. Similarly,

$$a_{ils}/a_{ilw} \simeq a_s/a_w \equiv g. \tag{A11}$$

In reality no two exposures are identical, so that f and g are calculated using average values of a_w, a_m and a_s.

Substituting expressions A10 and A11 into Equation A9 and simplifying, we obtain

$$2\left[\sum_{i=1}^{N} a_{ilw} \langle a_i \rangle/(N-1)\right] = \frac{2}{3} a_w^2 \left[(W+Mf+Sg)/(W+M+S)\right] \tag{A12}$$

and from Equation A7,

$$\sigma^2_{fl,lw} = \langle a \rangle^2 + a_w^2 \left[1 - \frac{2}{3} (W+Mf+Sg)/(W+M+S)\right]. \tag{A13}$$

This logic may be readily applied to any of the nine images, yielding

$$\sigma_{fl}^2 = \langle a \rangle^2 + \delta \cdot a^2, \tag{A14}$$

where the coefficient δ is a function only of exposure level:

$$\delta_w = 1 - \frac{2}{3}\,(W+Mf+Sg)/(W+M+S), \tag{A15}$$

$$\delta_m = 1 - \frac{2}{3}\,(\frac{W}{f} + M + \frac{Sg}{f})/(W+M+S), \tag{A16}$$

$$\delta_s = 1 - \frac{2}{3}\,(\frac{W}{g} + \frac{Mf}{g} + S)/(W+M+S). \tag{A17}$$

The derivation of $\langle a \rangle^2$, involving the evaluation of $\sum \langle a_i \rangle^2$ using Equation A8, will not be reproduced here, but leads to the following expression:

$$\begin{aligned} \langle a \rangle^2 = \frac{1}{9} \Big[& (W^2 + 2WMf)\ (a_{lw}^2 + a_{cw}^2 + a_{rw}^2) \\ & + (M^2 + \frac{2MSg}{f})\ (a_{lm}^2 + a_{cm}^2 + a_{rm}^2) \\ & + (S^2 + \frac{2WS}{g})\ (a_{ls}^2 + a_{cs}^2 + a_{rs}^2) \Big] / (W+M+S)^2. \end{aligned} \tag{A18}$$

The evaluation of Equation A7 for the case of complete de-correlation of FPN in all nine spectra, aligned as in Figure 3B, is not only simpler than in the foregoing discussion, but does not involve simplifying assumptions such as those in expressions A10 and A11. In this case sums over cross-terms such as in the last two terms of Equation A9 should vanish. This leads to an expression for σ_{fl} identical in form to Equation A14, but with

$$\delta = 1 - 2\ (C\langle FN \rangle / \sum C\langle FN \rangle), \tag{A19}$$

and

$$\langle a\rangle^2 = \sum(C\langle FN\rangle a)^2/(\sum C\langle FN\rangle)^2, \qquad \text{(A20)}$$

where the sums are taken over all nine images.

C. Fixed Pattern Noise, Second Difference Spectra

In calculating second difference spectra, we have shifted the L and R spectra back to their original offset positions in the large aperture, to re-align the FPN pattern (Figure 3E). We now describe sample points in terms of a new coordinate, j, which is fixed relative to the camera format and thus, is fixed relative to the FPN pattern (in contrast to coordinate i, which is fixed relative to the stellar line spectrum). In the example of Figure 3E, the L and R spectra are offset by $\pm$ 4 sample points relative to the C spectrum, so that for C, j=i, for L, j=i−4 and for R, j=i+4. To construct a second difference spectrum, we must know the value of the FPN amplitude in each first difference spectrum at point j, as well as the FPN amplitude at point j in the average of the first difference spectra. In the C first difference spectrum the FPN amplitude at point j is $(a_{i=j,c} - \langle a_{i=j}\rangle)$; in the L spectrum it is $(a_{j+4,l} - \langle a_{j+4}\rangle)$; and in the R spectrum it is $(a_{j-4,r} - \langle a_{j-4}\rangle)$. If we define X_j as the amplitude of FPN at point j of a second difference spectrum (for illustration we use the weak, left second difference spectrum), then

$$X_{jlw} = (a_{j+4,lw} - \langle a_{j+4}\rangle) - \bar{A}_j \qquad \text{(A21)}$$

where $\bar{A}_j$ is the FPN amplitude at point j in the average of first

difference spectra (Figure 3F), viz.,

$$\bar{A}_j = \frac{1}{9} \left[a_{j+4,1w} + a_{j+4,1m} + a_{j+4,1s} - 3 \langle a_{j+4} \rangle \right.$$
$$+ a_{jcw} + a_{jcm} + a_{jcs} - 3 \langle a_j \rangle$$
$$\left. + a_{j-4,rw} + a_{j-4,rm} + a_{j-4,rs} - 3 \langle a_{j-4} \rangle \right]. \qquad \text{(A22)}$$

However, the spectra are aligned so that, at any exposure level,

$$a_{j+4,1} = a_{jc} = a_{j-4,r}. \qquad \text{(A23)}$$

Substituting Equation A23 into A22 and A21 and simplifying, results in

$$X_{j1w} = \frac{2}{3} a_{jcw} - \frac{1}{3} a_{jcm} - \frac{1}{3} a_{jcs}$$
$$- \frac{2}{3} \langle a_{j+4} \rangle + \frac{1}{3} \langle a_j \rangle + \frac{1}{3} \langle a_{j-4} \rangle. \qquad \text{(A24)}$$

A corresponding expression can be derived for each of the nine second difference spectra (nine combinations of position and exposure level). The contribution of FPN to the standard deviation of a second difference spectrum is, in this case,

$$\sigma_{f2,1w} = \sqrt{\left[\sum_{j=1}^{N} X_{j1w}^2 \; / \; (N-1) \right]}. \qquad \text{(A25)}$$

The evaluation of expressions such as Equation A25 for each second difference spectrum involves squaring Equation A24 and evaluating the resulting 21 terms, including 15 cross-product terms. Twelve of these terms are themselves the sums of from 9 to 81 cross-product terms. This straightforward, though messy, procedure is greatly simplified by use of Equation A23 to determine which cross-terms consist of the product of

uncorrelated factors, the sum of which should vanish when taken over the large number of sample points of an order. For example, in evaluating $\sum \langle a_{j+4} \rangle \langle a_j \rangle$ we encounter the cross-term

$$\sum_{j=1}^{N} a_{j+4,cw}\, a_{jlm} = \sum_{j=1}^{N} a_{j+4,cw}\, a_{j-4,cm} \simeq 0, \tag{A26}$$

since $a_{j+4,c}$ and $a_{j-4,c}$ are assumed to be uncorrelated. On the other hand, the cross-term

$$\sum_{j=1}^{N} a_{j+4,cw}\, a_{jrm} = \sum_{j=1}^{N} a_{j+4,cw}\, a_{j+4,cm} \neq 0, \tag{A27}$$

since FPN fluctuations $a_{j+4,c}$ in images of different exposure level are assumed to be correlated. Following this reasoning, we reduce Equation A25 to terms in a_w, a_m and a_s (defined by Equation A5) and cross-terms involving sums over j of various products of a_{jcw}, a_{jcm} and a_{jcs}, with coefficients involving the weights W, M and S. Analogous to the derivation of $\sigma_{f1,1w}$ in terms of a_w (Equation A13), the derivation of $\sigma_{f2,1w}$ in terms of a_w becomes tractable only if we transform the resulting equation, using linear scaling factors $\underline{f}$ and $\underline{g}$ defined by Equations A10 and A11, respectively. The result for this specific example is

$$\sigma^2_{f2,1w} = \frac{2}{3} \langle a \rangle^2 + a_w^2 \left[\frac{1}{9} (2 - f - g)^2 - \frac{8}{81} (W+Mf+Sg)^2/(W+M+S)^2 \right]. \tag{A28}$$

Similar derivations yield expressions analogous to Equation A28 for all nine second difference spectra. As a check on this complicated procedure we note that setting f, g and the weights W, M and S to unity

reduces equation A28 to the same expression derived in a simpler version of this algorithm (Algorithm I discussed in § III). Also we find that, at any exposure level,

$$\sigma_{f2,l} = \sigma_{f2,r} > \sigma_{f2,c} \tag{A29}$$

as one would expect from Figure 3G.

The general solution for σ_{f2} is

$$\sigma_{f2}^2 = \frac{2}{3} \langle a \rangle^2 + \phi \cdot a^2, \tag{A30}$$

where the coefficient ϕ is a function both of offset position and of exposure level. That is,

$$\phi_{lw} = \phi_{rw} = Q_w \ (Z_w - K_l \ D), \tag{A31}$$

$$\phi_{cw} = Q_w \ (Z_w - K_c \ D), \tag{A32}$$

$$\phi_{lm} = \phi_{rm} = Q_m \ (Z_m - K_l \ D), \tag{A33}$$

$$\phi_{cm} = Q_m \ (Z_m - K_c \ D), \tag{A34}$$

and

$$\phi_{ls} = \phi_{rs} = Q_s \ (Z_s - K_l \ D), \tag{A35}$$

$$\phi_{cs} = Q_s \ (Z_s - K_c \ D), \tag{A36}$$

where

$$Q_w = 1, \ Q_m = \frac{1}{f^2} \ , \ Q_s = \frac{1}{g^2}, \tag{A37}$$

$$K_l = \frac{8}{81} \ , \ K_c = \frac{14}{81}, \tag{A38}$$

$$D = (W+Mf+Sg)^2/(W+M+S)^2, \tag{A39}$$

$$Z_w = \frac{1}{9}(2 - f - g)^2, \tag{A40}$$

$$Z_m = \frac{1}{9}(1 + g - 2f)^2, \tag{A41}$$

and

$$Z_s = \frac{1}{9}(1 + f - 2g)^2. \tag{A42}$$

D. Solution for Random and Fixed Pattern Noise

Combining Equations 2 (§ III) and A14 yields the overall rms noise amplitude of a first difference spectrum,

$$\sigma_1^2 = b^2 + \langle b\rangle^2 + \delta \cdot a^2 + \langle a\rangle^2. \tag{A43}$$

Similarly, combining Equations 4 and A30 yields the amplitude of a second difference spectrum,

$$\sigma_2^2 = b^2 + \langle b\rangle^2 + \langle\sigma_{r1}\rangle^2 + \phi \cdot a^2 + \frac{2}{3}\langle a\rangle^2. \tag{A44}$$

We thus have two equations in two unknowns, a and b, which can be solved simultaneously, using measured values of σ_1 and σ_2. The result is

$$a = \sqrt{\left[(\sigma_1^2 - \sigma_2^2 - \frac{1}{3}\langle a\rangle^2 + \langle\sigma_{r1}\rangle^2)/(\delta - \phi)\right]}, \tag{A45}$$

and

$$b = \sqrt{(\sigma_1^2 - \delta \cdot a^2 - \langle a\rangle^2 - \langle b\rangle^2)}. \tag{A46}$$

In practice we adopt an arbitrary set of nine starting values of a and nine starting values of b to utilize in calculating initial values of $\langle a\rangle$, $\langle b\rangle$ and $\langle\sigma_{r1}\rangle$ in the simple Algorithm I (described in § III). We then iterate Algorithm I until it converges to a final set of (a,b) values for the nine images. Convergence is rapid (15-20 iterations are required) and the resulting a and b values are unique, regardless of

what values are chosen for the starting set. These values of $\underline{a}$ and $\underline{b}$ are then adopted as the starting set for the more complex Algorithms II and III, described in this Appendix. Specifically they are used to calculate initial values of $\underline{f}$ and $\underline{g}$, the average ratios of FPN amplitudes (Equations A10 and A11), which initially are <u>not</u> allowed to vary as the algorithm iterates. (Attempts to allow f and g to vary with each iteration resulted in a very unstable and non-converging situation). This procedure yielded final $\underline{a}$-values from Algorithms II and III from which one could derive new values of $\underline{f}$ and $\underline{g}$, which differed somewhat from their starting values. To test the sensitivity of the solutions to $\underline{f}$ and $\underline{g}$, we then iterated the algorithm one additional time, using these new $\underline{f}$ and $\underline{g}$ values. In general the derived $\underline{a}$'s are insensitive to the adopted $\underline{f}$ and $\underline{g}$, varying by only 2-3% when $\underline{f}$ and $\underline{g}$ changed by about 20%. The derived $\underline{b}$'s are somewhat sensitive in that the smallest $\underline{b}$-values, at the largest average flux numbers, varied by as much as 20-30% for such large changes in $\underline{f}$ and $\underline{g}$. In the end we adopted (a,b) solutions derived from the final iteration with the updated $\underline{f}$ and $\underline{g}$-values.

TABLE 1

RECORD OF EXPOSURES

Star	Camera	Image	Offset Coordinates	Exposure (minutes)	Relative Velocity* Offset (km s^{-1})
21 Aql	LWR	15929	-37,-208	7.17	+37.8
		15930	-37,-208	2.60	+36.6
		15931	+5,-208	3.33	-16.3
		16066	+5,-208	12.17	-18.1
		16098	-16,-208	12.17	+7.7
		16099	+5,-208	7.00	-23.0
		16100	-37,-208	7.00	+32.2
		16110	-16,-208	3.33	0.0
		16111	-16,-208	7.00	+0.3
	SWP	19969	-37,-208	3.40	-23.3
		19970	+5,-208	5.00	+32.7
		19971	-16,-208	7.35	+9.5
		20143	+5,-208	18.67	+23.0
		20144	-37,-208	16.60	-32.8
		20165	-16,-208	15.50	-0.7
		20166	+5,-208	7.70	+26.0
		20175	-37,-208	8.33	-28.6
		20176	-16,-208	5.20	0.0
o Peg	LWR	15943	-37,-208	4.50	+26.3
		15944	+5,-208	4.92	-34.3
		16055	-37,-208	18.00	+20.4
		16056	+5,-208	18.00	-27.4
		16057	+5,-208	12.83	-30.8
		16058	-37,-208	12.83	+22.9
		16059	-16,-208	5.90	0.0
		16101	-16,-208	18.90	-5.0
		16102	-16,-208	11.75	-3.8
	SWP	19984	-37,-208	6.50	-24.7
		19985	+5,-208	6.83	+27.9
		19989	-16,-208	37.00	-1.4
		20128	-37,-208	39.00	-29.6
		20129	+5,-208	40.00	+24.1
		20130	+5,-208	16.33	+24.7
		20131	-37,-208	16.00	-31.5
		20132	-16,-208	8.83	0.0
		20167	-16,-208	16.33	+0.9
θ Leo	LWR	15932	-37,-208	1.50	+32.9
		15933	+5,-208	1.50	-20.7
		15934	-37,-208	3.08	+32.4
		15935	-16,-208	5.50	+8.5
		15946	+5,-208	2.60	-23.7
		16103	-37,-208	5.70	+26.5
		16113	+5,-208	6.17	-19.0
		16114	-16,-208	3.80	+2.1
		16115	-16,-208	1.50	0.0

TABLE 1 - *Continued*

Star	Camera	Image	Offset Coordinates	Exposure (minutes)	Relative Velocity* Offset (km s^{-1})
θ Leo	SWP	19972	-37,-208	2.83	-30.0
		19973	+5,-208	2.33	+26.4
		19974	-37,-208	4.00	-32.7
		19975	-16,-208	17.50	-4.2
		20169	-16,-208	17.75	-3.9
		20170	-37,-208	16.00	-33.6
		20178	-16,-208	5.27	-5.9
		20179	-16,-208	2.75	0.0
		20180	+5,-208	5.00	+26.5

*Includes positional offset and differential spacecraft velocity.

TABLE 2

DIRECT NOISE MEASUREMENTS IN "LINE-FREE" INTERVALS OF CO-ADDED SPECTRA OF "WEAK-LINED" STARS

Star	Camera	Number of Co-Added Images	Wavelength Interval (Å)	Measured σ
HD 109995	SWP	8	2005.5-2006.1	0.016
			1941.5-1942.8	0.015
			1740.5-1741.3	0.021
			1709.9-1710.5	0.022
			1700.8-1701.6	0.022
			1614.8-1615.3	0.014
			1606.7-1607.2	0.024
	LWP	6	2937.1-2939.0	0.015
			2823.5-2824.7	0.011
			2601.8-2602.6	0.013
21 Aql	SWP	9	1908.5-1909.5	0.008
			1836.3-1837.3	0.021*
			1796.2-1796.6	0.008
			1689.1-1689.7	0.017
			1573.2-1573.7	0.026
			1517.2-1517.7	0.017
			1459.5-1460.1	0.022
			1439.8-1440.2	0.029
			1388.8-1389.5	0.027*
	LWR	9	2772.3-2773.7	0.018
			2601.7-2602.5	0.018
			2595.7-2597.7	0.031*
			2535.9-2536.4	0.015

*Possible weak lines present

TABLE 3

FITTING PARAMETERS FOR
$\langle FPN \rangle = [P^2 + Q^2 \langle FN \rangle^{2R}]^{0.5}$

Interval (Å)	P	Q	R
1474-1488	550	0.087	1.000
(SWP 93)	0*	0.104	0.988
1651-1670	0*	0.478	0.753
(SWP 83)			
2256-2276	0*	2.153	0.702
(LWR 102)			
2395-2418	0*	0.993	0.741
(LWR 96)			

* When the background is not directly observed, its contribution is subsumed in parameters Q and R, and P is set to zero. <FPN> is in flux number units; divide by <FN> to convert to fractional noise-to-signal ratio.

TABLE 4

FITTING PARAMETERS FOR
$[\langle FPN \rangle^2 + \langle RN \rangle^2]^{0.5} = D + E \langle FN \rangle$

Wavelength Interval(Å)	D	E
1474-1488	558	0.0844
(SWP 93)		
1651-1670	586	0.0348
(SWP 83)		
2256-2276	1310	0.0659
(LWR 102)		
2395-2418	1571	0.0355
(LWR 96)		

TABLE 5

FIXED PATTERN, RANDOM, AND TOTAL NOISE
IN CO-ADDED SPECTRA

Wavelength Interval (Å)	Star	Algorithm II <a>	<b>	Total	Algorithm III <a>	<b>	Total
2256-2276 (LWR 102)	21 Aql	0.086	0.022	0.089	0.044	0.026	0.051
	θ Leo	0.086	0.024	0.089	0.041	0.023	0.047
	o Peg	0.079	0.019	0.081	0.037	0.021	0.043
2395-2418 (LWR 96)	21 Aql	0.047	0.016	0.050	0.022	0.019	0.029
	θ Leo	0.054	0.018	0.057	0.026	0.021	0.033
	o Peg	0.055	0.016	0.057	0.026	0.019	0.032
1474-1488 (SWP 93)	21 Aql	0.061	0.018	0.064	0.031	0.022	0.038
	θ Leo	0.082	0.028	0.087	0.048	0.018	0.051
	o Peg	0.079	0.023	0.082	0.041	0.020	0.046
1555-1575 (SWP 88)	o Peg	0.058	0.020	0.061	0.029	0.018	0.034
1651-1670 (SWP 83)	21 Aql	0.023	0.014	0.027	0.011	0.015	0.019
	o Peg	0.035	0.015	0.038	0.019	0.017	0.025

TABLE 6

ESTIMATED TOTAL NOISE AT THE CONTINUUM LEVEL

Star	Wavelength Interval(Å)	$\overline{\langle FN \rangle}$*	$\bar{F}/F_c$	Contin. Noise /Mean Noise	Noise at Continuum Alg. II	Alg.III
21 Aql	1651-1670	24,125	0.80	0.885	0.024	0.017
	1474-1488	22,100	0.80	0.955	0.061	0.036
	2395-2418	30,048	0.80	0.875	0.044	0.025
	2256-2276	18,414	0.80	0.905	0.081	0.046
o Peg	1651-1670	19,577	0.64	0.833	0.032	0.021
	1555-1575	14,299	0.61	0.859	0.052	0.029
	1474-1488	12,546	0.58	0.853	0.070	0.039
	2395-2418	26,075	0.68	0.786	0.045	0.025
	2256-2276	18,340	0.68	0.832	0.067	0.036
θ Leo	1474-1488	15,367	0.59	0.899	0.078	0.046
	2395-2418	26,793	0.67	0.789	0.045	0.026
	2256-2276	19,044	0.67	0.830	0.074	0.039

*Mean average flux level associated with co-added spectrum;

$\overline{\langle FN \rangle} = \Sigma C\langle FN \rangle / \Sigma C$, summed over all spectra in the co-add.

REFERENCES

Adelman, S. J., and Leckrone, D. S. 1985, NASA IUE Newsletter, 28, 35.

Kinney, A. L., Bohlin, R. C., and Neill, J. D. 1988, NASA IUE Newsletter, in press.

Linde, P., and Dravins, D. 1988, ESA IUE Newsletter, 29, 11.

Nichols-Bohlin, J. 1988, NASA IUE Newsletter, in press.

Turnrose, B. E., and Thompson, R. W. 1984, "International Ultraviolet Explorer Image Processing Manual Version 2.0 (New Software)", Computer Sciences Corporation Report TM-84/6058.

West, K., and Shuttleworth, T. 1981, ESA IUE Newsletter, 12, 27.

York, D. G., and Jura, M. 1982, Ap. J., 254, 88.

FIGURE LEGENDS

Fig. 1. - Comparison of single, small aperture, high dispersion spectrum (top) of the B7 V star π Cet near Si II, multiplet UV 2, to the co-addition of nine such spectra (bottom). The improvement in the signal-to-noise ratio is slight due to the presence of coherent, fixed pattern noise.

Fig. 2. - Comparison of single, large aperture, high dispersion spectrum (top) of the B7 IV star 21 Aql near Si II, multiplet UV 2, to the co-addition of nine spectra, observed at three offset positions in the large aperture (bottom). Note the substantial improvement in the signal-to-noise ratio due to the "randomization" of fixed pattern noise.

Fig. 3. - Simplified model of the behavior of fixed pattern noise amplitude as images observed in offset positions L (left), C (center), and R (right) are shifted, averaged, and processed to produce first and second difference spectra as described in §III.

Fig. 4. - Illustrative example of the computation of an actual first difference spectrum. At the top is shown the original spectrum from image SWP 20175, overplotted with a co-addition of nine similar large aperture images taken at three offset positions. The lower plot is the difference between the two. The standard deviation in the first

difference spectrum, σ_1, is computed relative to a least-squares linear fit to the lower plot.

Fig. 5. - Measured values of the standard deviation of first difference spectra versus average flux number for four IUE orders.

Fig. 6. - Measured values of the standard deviation of second difference spectra versus average flux number for four IUE orders.

Fig. 7. - Average fixed pattern noise amplitude within the indicated wavelength intervals, expressed as a fractional noise-to-signal ratio, versus average flux number for four IUE orders. The dashed curves are best fits through the data expressed by Equation 6 and the fitting parameters of Table 3. The least squares fits through intermediate and high flux number data are taken from the log-log plots of Figure 8.

Fig. 8. - Log-log plots of average fixed pattern noise amplitude, in absolute flux number units, versus average flux number. At intermediate and high flux numbers the data follow a linear relation. The solid lines illustrate linear least squares fits through the data. The data for order SWP 93 extend to sufficiently low FN that a bifurcation can be seen. At low FN the noise is dominated by an "additive" background compoonent.

Fig. 9. - Average random noise amplitude within the indicated wavelength intervals, expressed as a fractional noise-to-signal ratio, versus

average flux number for four IUE orders. The dashed curves are best fits through the data expressed by Equation 7. As discussed in §IV, the same fitting parameters work for all four orders if one corrects for an apparent zero-point error in the flux number scale of the LWR orders.

Fig. 10. - Total noise versus average flux number within the indicated wavelength intervals of four IUE orders. The plotted data points and linear least squares fits through them (solid lines) are in units of absolute flux number (left vertical scale). The dashed curves are the corresponding fractional noise-to-signal ratios (right vertical scale). The vertical arrows indicate our best estimate of the average flux numbers in ideally exposed individual spectra of sharp-lined stars in which the ratio of average flux level to the continuum is about 0.6-0.8.

AUTHORS' ADDRESSES

Dr. Saul J. Adelman
Department of Physics
The Citadel
Charleston, SC 29407

Dr. David S. Leckrone
Code 681
Laboratory for Astronomy and Solar Physics
NASA, Goddard Space Flight Center
Greenbelt, MD 20771

Please send proofs to Dr. Leckrone

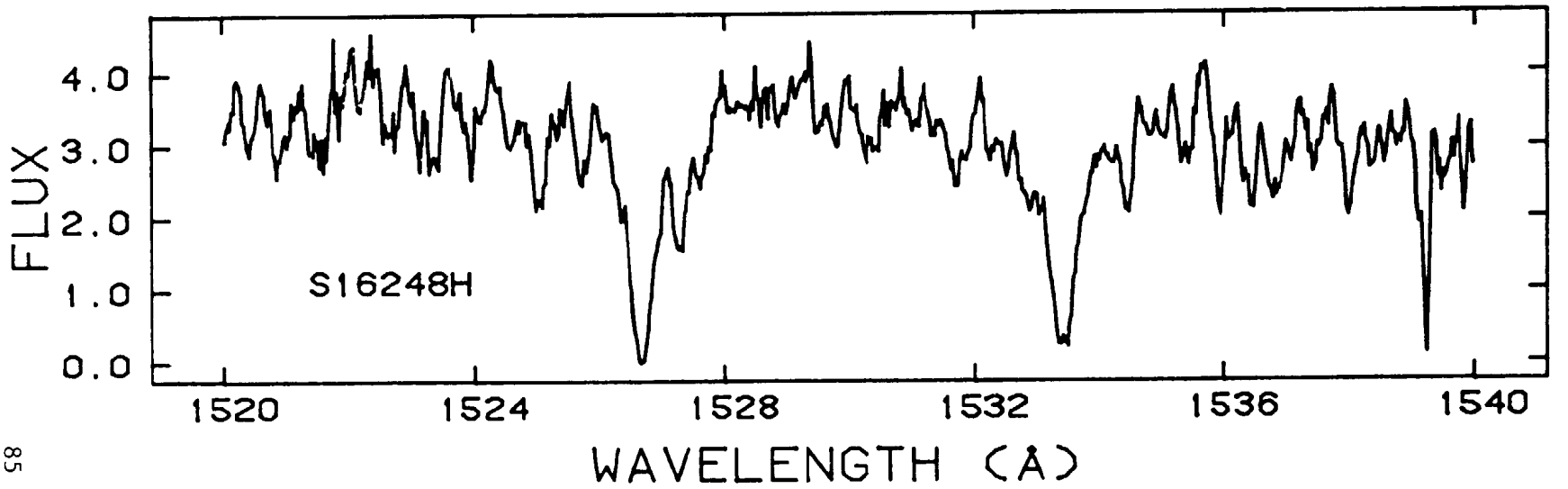
FLUX
4.0
3.0
2.0
1.0
0.0
S16248H
1520
1524
1528
1532
1536
1540
WAVELENGTH (Å)

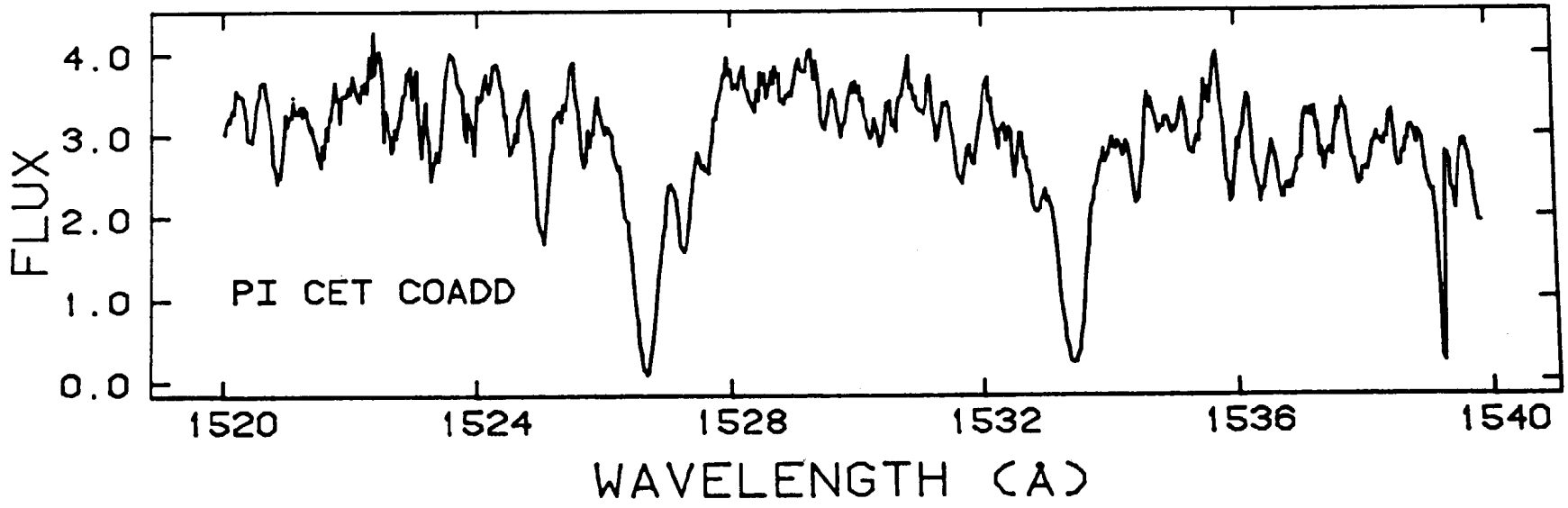
FLUX
4.0
3.0
2.0
1.0
0.0
PI CET COADD
1520
1524
1528
1532
1536
1540
WAVELENGTH (Å)

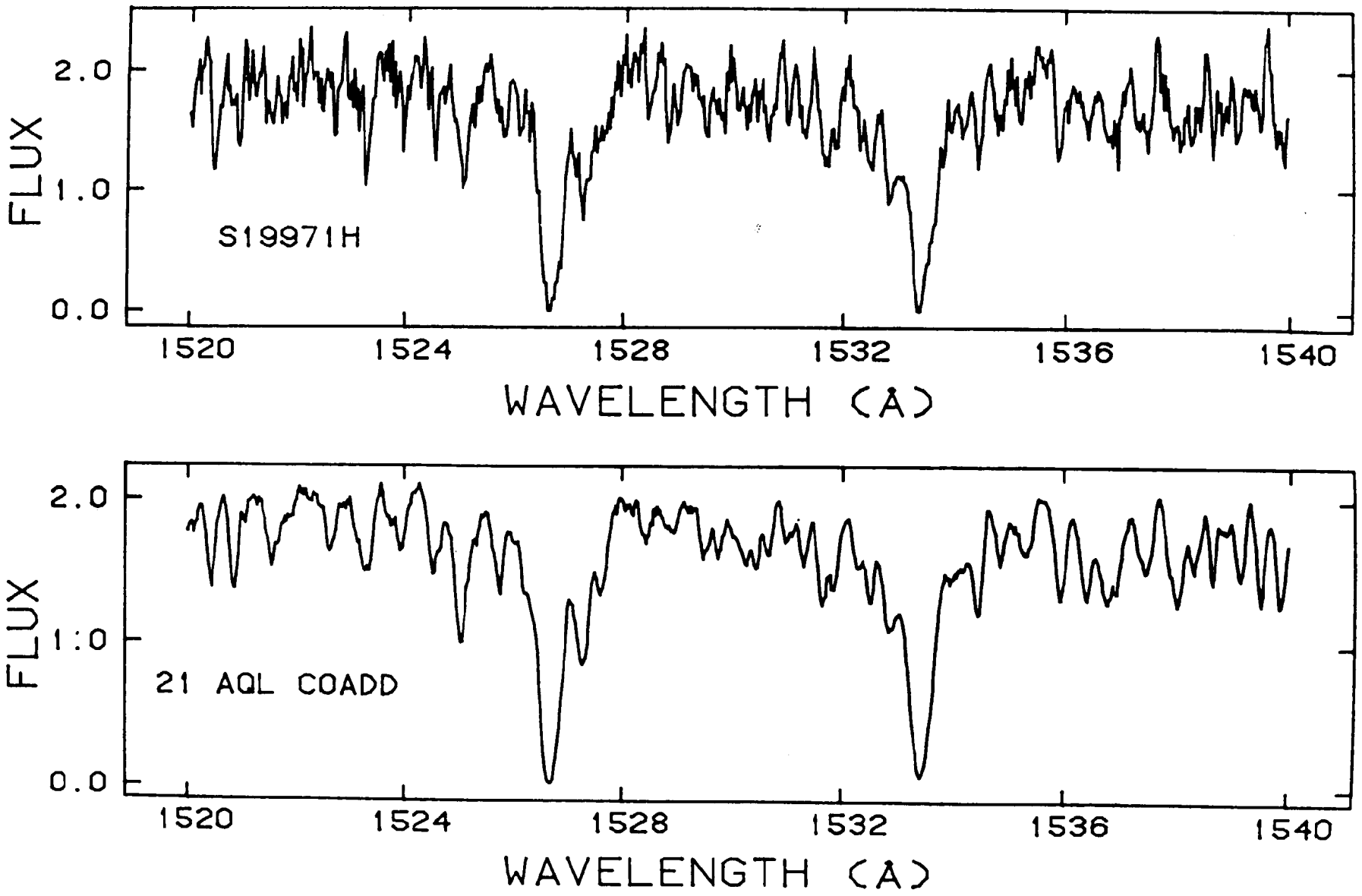
S19971H
FLUX
2.0
1.0
0.0
1520
1524
1528
1532
1536
1540
WAVELENGTH (Å)
21 AQL COADD
FLUX
2.0
1:0
0.0
1520
1524
1528
1532
1536
1540
WAVELENGTH (Å)

A. FPN Pattern of Offset Spectra

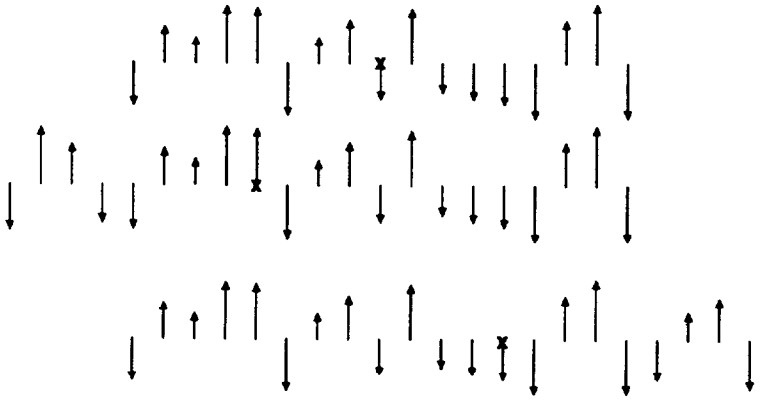

B. Aligned Spectra

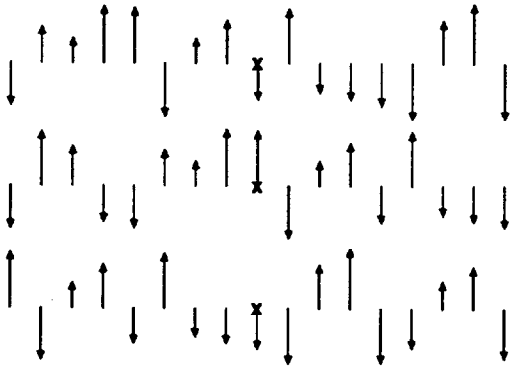

C. Average of Aligned Spectra

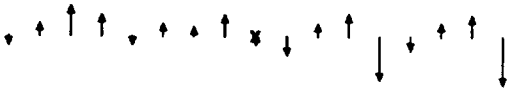

D. First Difference Spectra

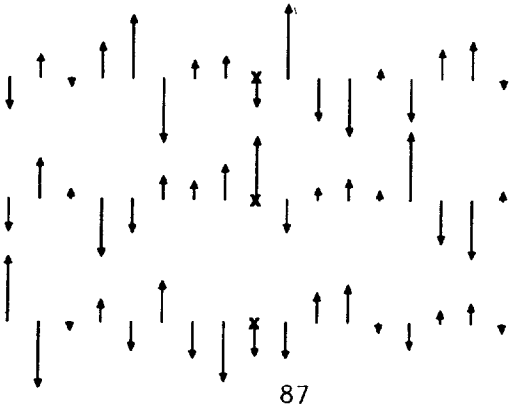

E. First Difference Spectra Offset to Original Position

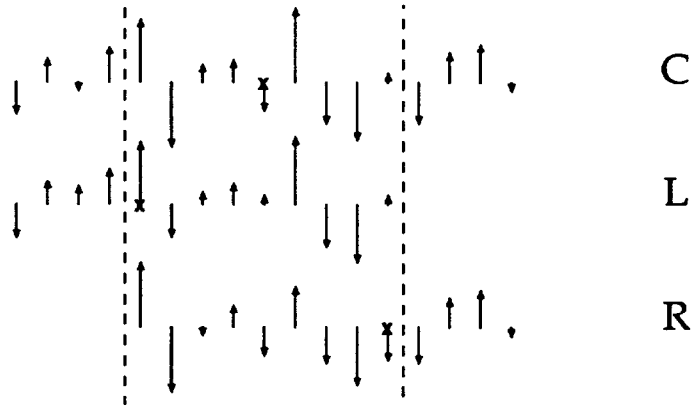

F. Average of First Difference Spectra (Central Points Only)

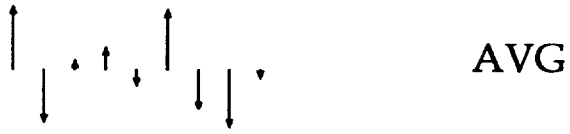

G. Second Difference Spectra

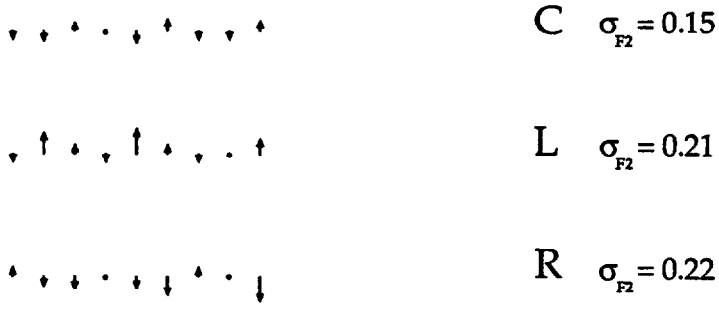

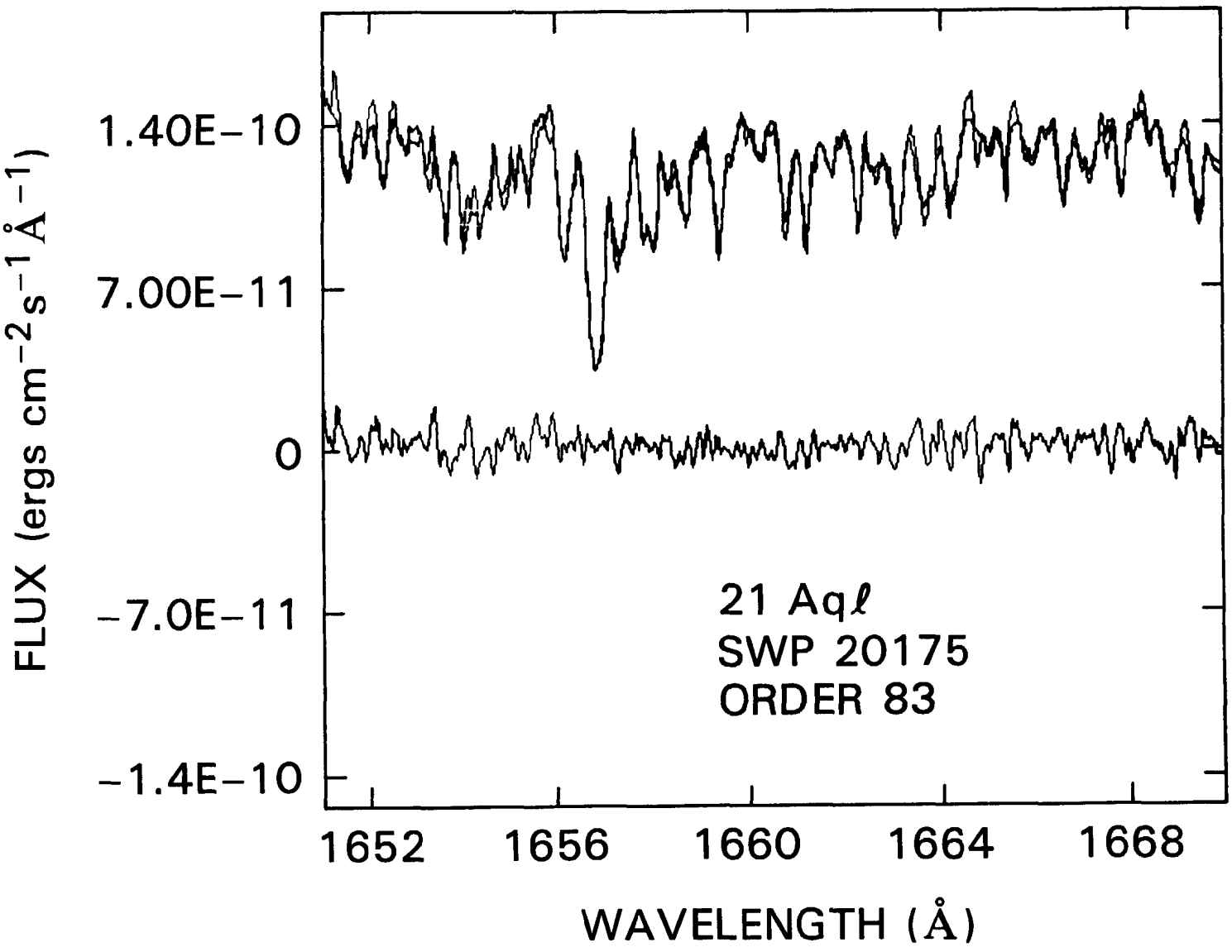
1.40E-10
7.00E-11
0
-7.0E-11
-1.4E-10
FLUX (ergs cm^{-2}s^{-1}Å^{-1})
21 Aqℓ
SWP 20175
ORDER 83
1652
1656
1660
1664
1668
WAVELENGTH (Å)

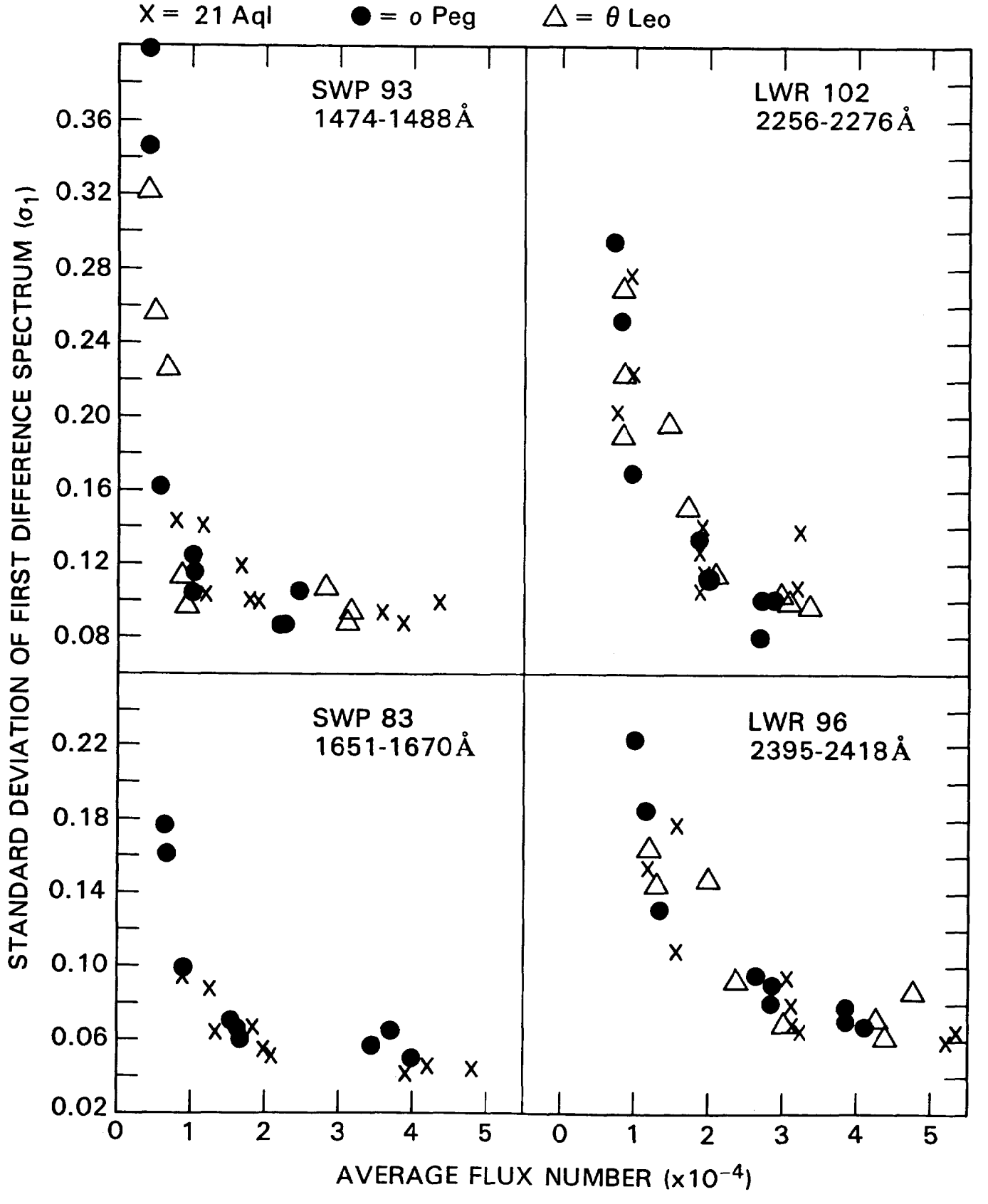
X = 21 Aql
● = o Peg
△ = θ Leo
SWP 93
1474-1488Å
LWR 102
2256-2276Å
SWP 83
1651-1670Å
LWR 96
2395-2418Å
STANDARD DEVIATION OF FIRST DIFFERENCE SPECTRUM (σ1)
AVERAGE FLUX NUMBER (x10⁻⁴)
0.36
0.32
0.28
0.24
0.20
0.16
0.12
0.08
0.22
0.18
0.14
0.10
0.06
0.02
0
1
2
3
4
5

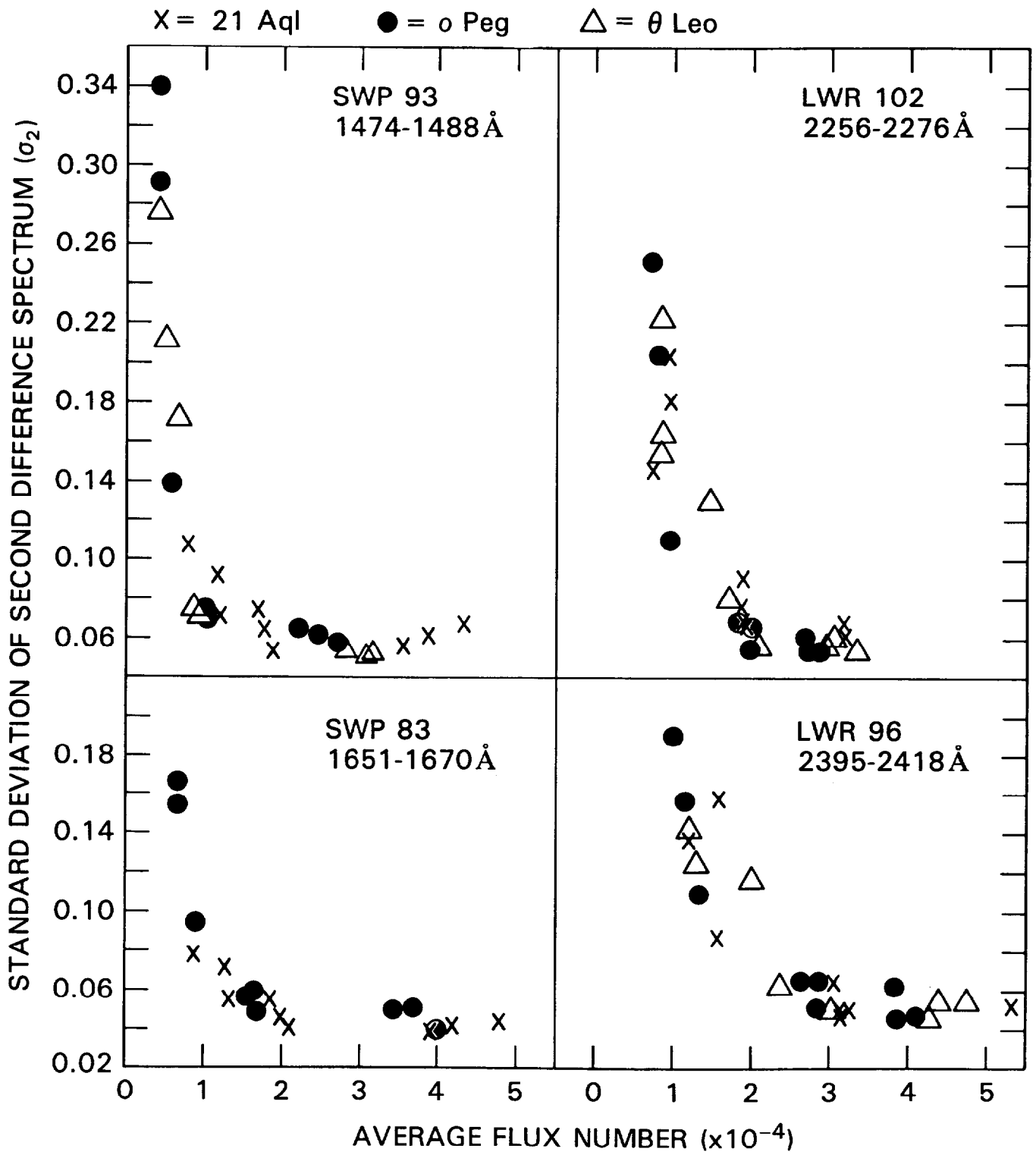
X = 21 Aql
● = o Peg
△ = θ Leo
SWP 93
1474-1488Å
LWR 102
2256-2276Å
SWP 83
1651-1670Å
LWR 96
2395-2418Å
STANDARD DEVIATION OF SECOND DIFFERENCE SPECTRUM (σ_2)
AVERAGE FLUX NUMBER (x10^{-4})
0.34
0.30
0.26
0.22
0.18
0.14
0.10
0.06
0.18
0.14
0.10
0.06
0.02
0
1
2
3
4
5

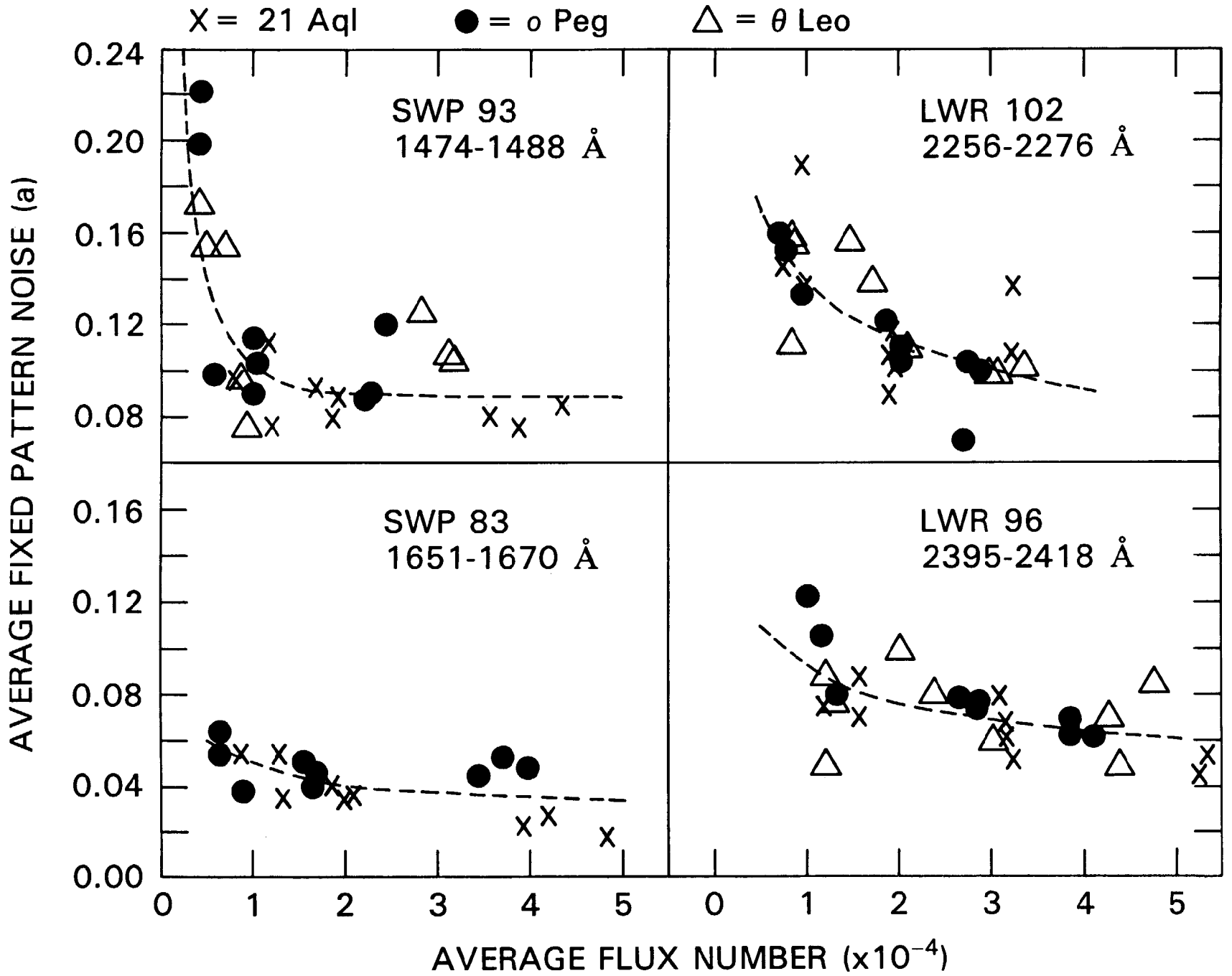
X = 21 Aql
● = o Peg
△ = θ Leo
SWP 93
1474-1488 Å
LWR 102
2256-2276 Å
SWP 83
1651-1670 Å
LWR 96
2395-2418 Å
AVERAGE FIXED PATTERN NOISE (a)
AVERAGE FLUX NUMBER (x10⁻⁴)
0.24
0.20
0.16
0.12
0.08
0.04
0.00
0
1
2
3
4
5

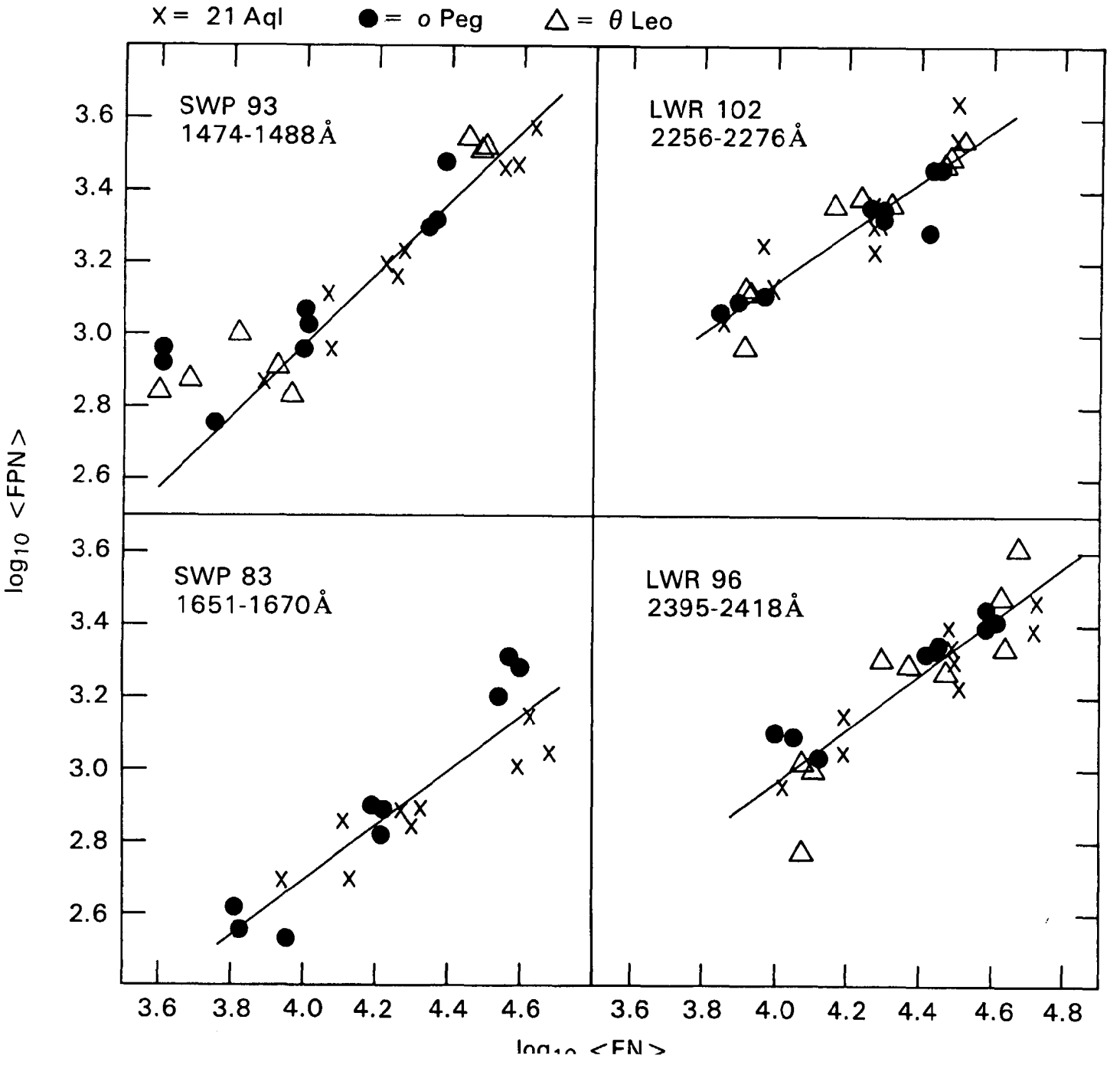
X = 21 Aql
● = o Peg
△ = θ Leo
SWP 93
1474-1488Å
LWR 102
2256-2276Å
SWP 83
1651-1670Å
LWR 96
2395-2418Å
log10 <FPN>
log10 <FN>
3.6
3.4
3.2
3.0
2.8
2.6
3.8
4.0
4.2
4.4
4.6
4.8

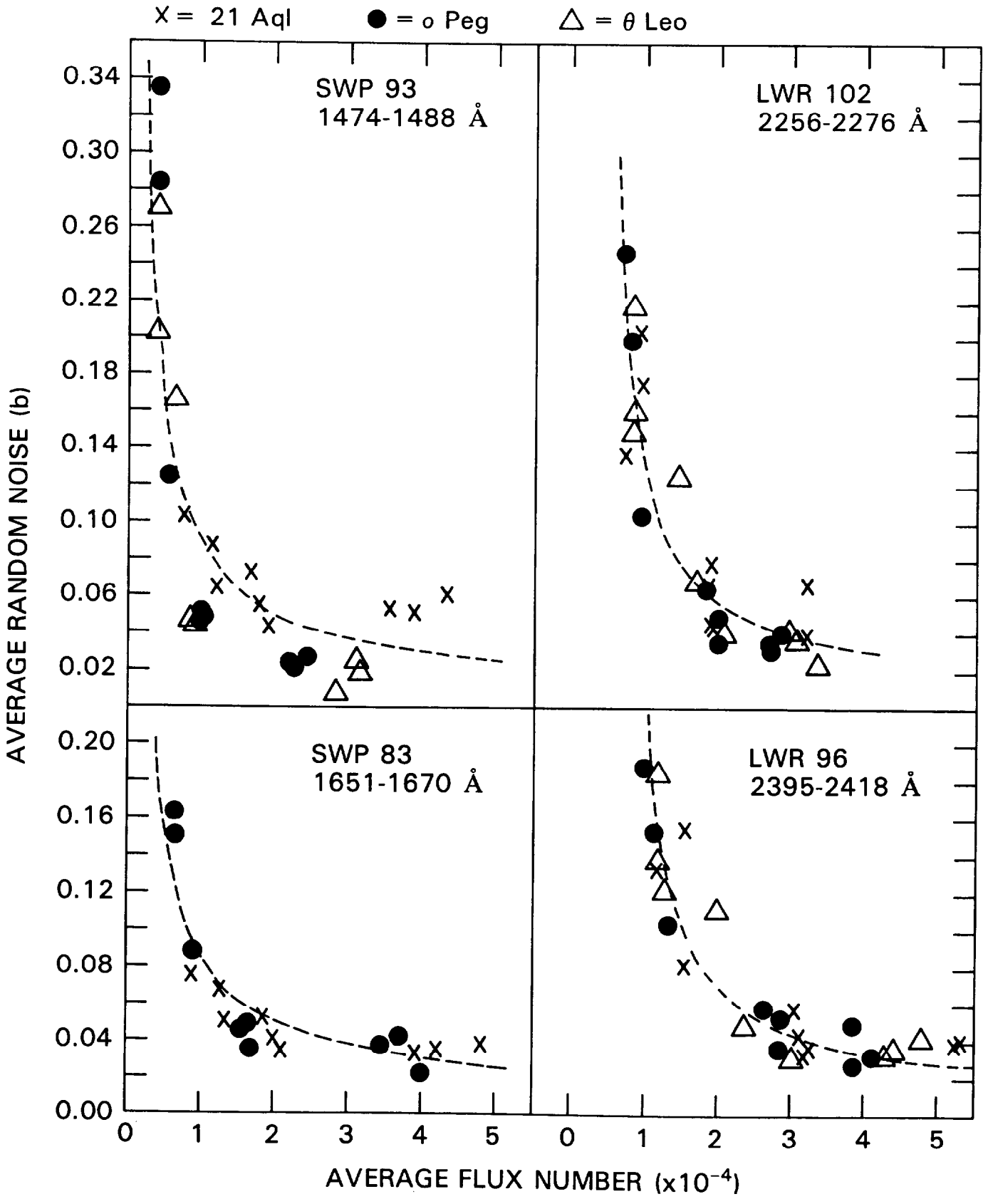
X = 21 Aql
● = o Peg
△ = θ Leo
SWP 93
1474-1488 Å
LWR 102
2256-2276 Å
SWP 83
1651-1670 Å
LWR 96
2395-2418 Å
AVERAGE RANDOM NOISE (b)
AVERAGE FLUX NUMBER (x10⁻⁴)
0.34
0.30
0.26
0.22
0.18
0.14
0.10
0.06
0.02
0.20
0.16
0.12
0.08
0.04
0.00
0
1
2
3
4
5

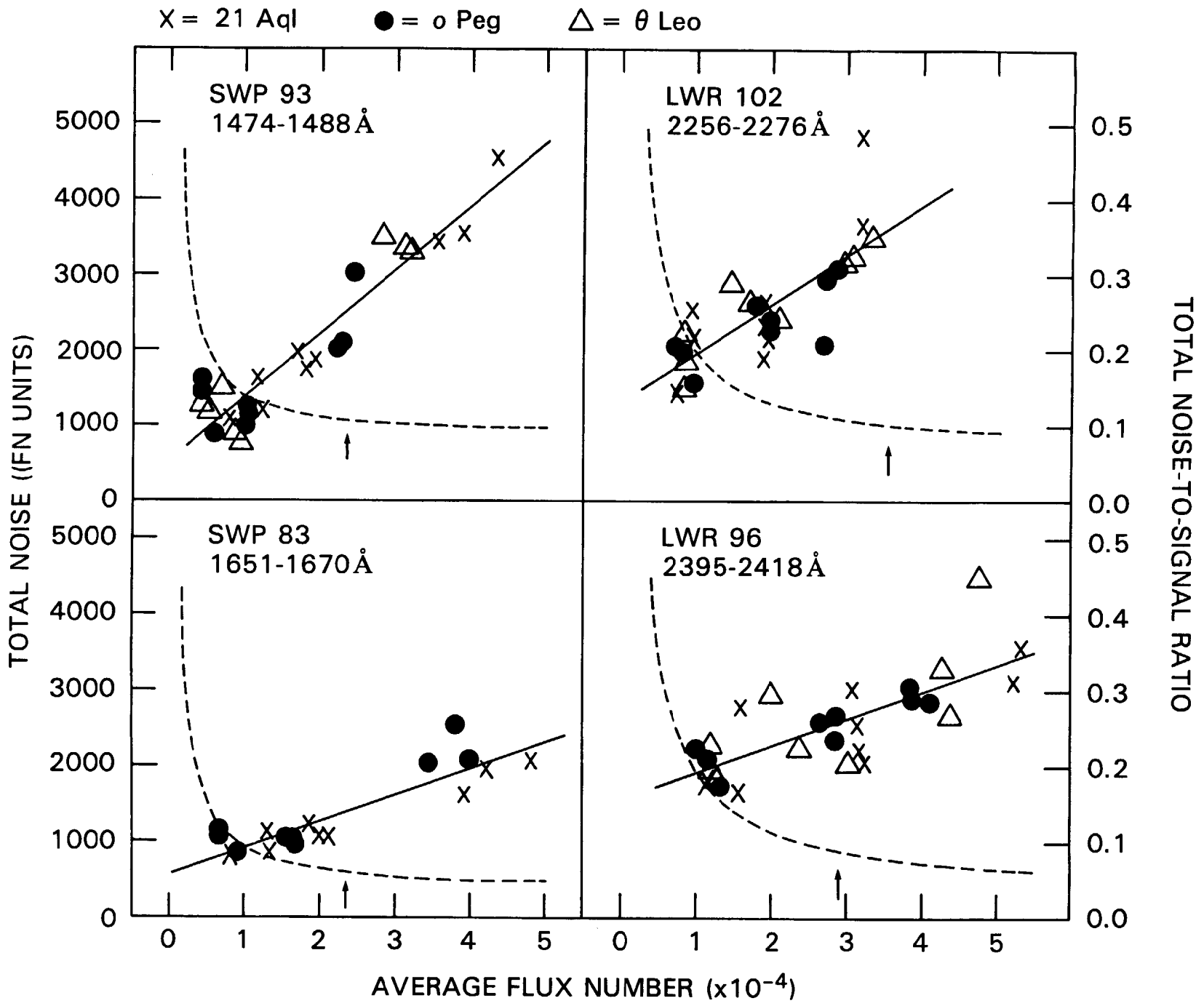
X = 21 Aql
● = o Peg
△ = θ Leo
SWP 93
1474-1488Å
LWR 102
2256-2276Å
SWP 83
1651-1670Å
LWR 96
2395-2418Å
TOTAL NOISE ((FN UNITS)
TOTAL NOISE-TO-SIGNAL RATIO
AVERAGE FLUX NUMBER (x10⁻⁴)
0
1000
2000
3000
4000
5000
0.0
0.1
0.2
0.3
0.4
0.5
1
2
3
4
5